

EUROPEAN ORGANISATION FOR NUCLEAR RESEARCH (CERN)



Submitted to: Eur. Phys. J. C

CERN-EP-2022-087
1st July 2022

Measurements of W^+W^- production in decay topologies inspired by searches for electroweak supersymmetry

The ATLAS Collaboration

This paper presents a measurement of fiducial and differential cross-sections for W^+W^- production in proton–proton collisions at $\sqrt{s} = 13$ TeV with the ATLAS experiment at the Large Hadron Collider using a dataset corresponding to an integrated luminosity of 139 fb^{-1} . Events with exactly one electron, one muon and no hadronic jets are studied. The fiducial region in which the measurements are performed is inspired by searches for the electroweak production of supersymmetric charginos decaying to two-lepton final states. The selected events have moderate values of missing transverse momentum and the ‘stransverse mass’ variable m_{T2} , which is widely used in searches for supersymmetry at the LHC. The ranges of these variables are chosen so that the acceptance is enhanced for direct W^+W^- production and suppressed for production via top quarks, which is treated as a background. The fiducial cross-section and particle-level differential cross-sections for six variables are measured and compared with two theoretical SM predictions from perturbative QCD calculations.

1 Introduction

Measurements of W^+W^- (referred to hereafter as WW) production provide important tests of the electroweak (EWK) gauge structure of the Standard Model (SM) of particle physics, and WW production is also an important background process in searches for physics beyond the SM (BSM physics). In searches for supersymmetry [1–6] (SUSY) where WW events are a significant background, a semi-data-driven approach is often taken, that involves normalising the simulated Monte Carlo (MC) samples to data in a control region (CR), designed to be kinematically similar to the search regions but enriched in SM WW production. Significant deviations of these scaling factors from unity suggest mismodelling in the phase space targeted by the search, but it can be difficult to make comparisons with the level of agreement observed in precision SM measurements because the scaling factors refer to detector-level quantities which are subject to mis-measurement and inefficiency. Producing "unfolded" particle-level measurements, which are corrected for these effects and can directly be compared with the prediction of a MC event generator, in event topologies associated with search results is a novel way to address this whilst simultaneously extending the programme of precision SM measurements at the LHC. The ATLAS experiment [7] has previously reported differential measurements of $t\bar{t}$ and Z +jets production in regions related to a search for leptoquarks in dilepton+dijet events [8]. This paper presents the first effort to measure WW production cross-sections in topologies associated with SUSY searches.

Inclusive and fiducial WW production cross-sections have been measured in proton–proton (pp) collisions at $\sqrt{s} = 7$ TeV [9, 10], 8 TeV [11–13] and 13 TeV [14–17] at the LHC, as well as in e^+e^- collisions at LEP [18] and in $p\bar{p}$ collisions at the Tevatron [19–21]. This analysis complements existing ATLAS measurements of WW production at 13 TeV in 0-jet events [15] and in ≥ 1 -jet events [16] by measuring differential cross-sections in a fiducial region kinematically close to the WW control region used in a previous search for electroweak production of supersymmetric charginos or sleptons [22]. That search targeted electroweak production of SUSY particles decaying into final states with two leptons (electrons or muons) and missing transverse momentum using 139 fb^{-1} of pp collisions at 13 TeV collected during Run 2 of the LHC and is referred to hereafter as the ‘EWK $2\ell+0$ -jets search’. In that search, WW production was the main background process and the associated theoretical uncertainties were among the dominant systematic uncertainties in the search regions. The present measurement targets event topologies with higher values of the dilepton invariant mass, $m_{e\mu}$, and the magnitude of the missing transverse momentum, E_T^{miss} , than were used in previous measurements, and can thus be used to provide additional constraints on BSM physics, and probe the expected SM backgrounds for future searches.

The $WW \rightarrow e^\pm\nu\mu^\mp\nu$ decay channel is studied in events with no identified jets with a transverse momentum $p_T > 20\text{ GeV}$ and pseudorapidity $|\eta| < 2.4$,¹ and with E_T^{miss} between 60 and 80 GeV. Missing transverse momentum is calculated so as to represent the momentum imbalance in the plane transverse to the colliding beams. High values of E_T^{miss} can be produced when weakly interacting neutral particles escape the detector unseen, and E_T^{miss} is thus an important variable in many BSM searches. This analysis also imposes requirements on the dilepton invariant mass that are more stringent than those in the 36 fb^{-1} $WW+0$ -jet measurement [15]. The dominant background process is top-quark production ($t\bar{t}$ and single-top Wt), which is estimated using the same data-driven method as was used in the EWK $2\ell+0$ -jets search. The measurements are performed in a fiducial phase space close to the geometric and kinematic acceptance of

¹ ATLAS uses a right-handed coordinate system with its origin at the nominal interaction point (IP) in the centre of the detector and the z -axis along the beam pipe. The x -axis points from the IP to the centre of the LHC ring, and the y -axis points upward. Cylindrical coordinates (r, ϕ) are used in the transverse plane, ϕ being the azimuthal angle around the z -axis. The pseudorapidity is defined in terms of the polar angle θ as $\eta = -\ln \tan(\theta/2)$

the experimental analysis. Differential cross-section measurements are performed for six variables, which are the same as those considered in the 36 fb^{-1} $WW+0\text{-jet}$ measurement [15]:

- The rapidity of the dilepton system, $|y_{e\mu}|$.
- The azimuthal separation between the two leptons, $|\Delta\phi_{e\mu}|$.
- The angular variable $\cos\theta^* = |\tanh(\Delta y(e\mu)/2)|$, which is longitudinally boost invariant and sensitive to the spin structure of the produced dileptons [23], and where $\Delta y(e\mu)$ is the difference between the electron and muon rapidities.
- The transverse momentum of the leading lepton, $p_T^{\text{lead}\ell}$.
- The invariant mass of the dilepton system, $m_{e\mu}$.
- The transverse momentum of the dilepton system, $p_T^{e\mu}$.

In this paper, $|y_{e\mu}|$, $|\Delta\phi_{e\mu}|$ and $\cos\theta^*$ are referred to collectively as ‘angular’ variables, as they probe angular correlations and are sensitive to the spin structure of the WW production system, and $p_T^{\text{lead}\ell}$, $m_{e\mu}$ and $p_T^{e\mu}$ are referred to collectively as ‘scale’ variables, as they characterise the energy scale of the process.

The rest of this paper is structured as follows. First, Section 2 describes the ATLAS detector and then Section 3 presents the analysis that is performed to measure the fiducial and differential cross-sections. This includes the data and MC samples used, the reconstructed-object definitions and event selections used to define the detector-level signal regions, and the SM background estimation, as well as the systematic uncertainties considered and the unfolding techniques used to correct detector-level information back to particle level. Finally, the results are reported in Section 4, and Section 5 presents the conclusions.

2 ATLAS detector

The ATLAS experiment at the LHC is a multipurpose particle detector with a forward–backward symmetric cylindrical geometry and a near 4π coverage in solid angle. It consists of an inner tracking detector surrounded by a thin superconducting solenoid providing a 2 T axial magnetic field, electromagnetic and hadron calorimeters, and a muon spectrometer. The inner tracking detector covers the pseudorapidity range $|\eta| < 2.5$. It consists of silicon pixel, silicon microstrip, and transition radiation tracking detectors. Lead/liquid-argon (LAr) sampling calorimeters provide electromagnetic (EM) energy measurements with high granularity. A steel/scintillator-tile hadron calorimeter covers the central pseudorapidity range ($|\eta| < 1.7$). The endcap and forward regions are instrumented with LAr calorimeters for both the EM and hadronic energy measurements up to $|\eta| = 4.9$. The muon spectrometer surrounds the calorimeters and is based on three large superconducting air-core toroidal magnets with eight coils each. The field integral of the toroids ranges between 2.0 and 6.0 T m across most of the detector. The muon spectrometer includes a system of precision tracking chambers and fast detectors for triggering. A two-level trigger system is used to select events. The first-level trigger is implemented in hardware and uses a subset of the detector information to accept events at a rate below 100 kHz. This is followed by a software-based trigger that reduces the accepted event rate to 1 kHz on average depending on the data-taking conditions. An extensive software suite [24] is used in the reconstruction and analysis of real and simulated data, in detector operations, and in the trigger and data acquisition systems of the experiment.

3 Analysis

3.1 Data and simulated event samples

This analysis uses pp collision data at a centre-of-mass energy of $\sqrt{s} = 13$ TeV collected by the ATLAS detector during the second data-taking run of the LHC, which took place between 2015 and 2018. After applying standard data-quality requirements for LHC and detector operations [25], this dataset corresponds to a total integrated luminosity of 139 fb^{-1} with an uncertainty of 1.7% [26], obtained using the LUCID-2 sub-detector [27] for the primary luminosity measurements. Candidate events were selected by a trigger that required at least one electron–muon pair [28, 29]. The trigger-level thresholds for the p_T of the leptons were 17 GeV for the electron and 14 GeV for the muon. The thresholds applied in the lepton offline selection ensured that trigger efficiencies are constant in the relevant phase space.

Simulated MC event samples are used for the SM background estimates and to correct the signal distributions for detector effects. These were processed through a full simulation of the ATLAS detector [30] based on GEANT4 [31] and reconstructed with the same algorithms as those used for the data. The generation of the simulated event samples includes the effect of multiple pp interactions per bunch crossing (pile-up), as well as changes in detector response because of interactions in bunch crossings before or after the one containing the hard interaction. Differences between data and simulation in the lepton reconstruction efficiency, energy scale, energy resolution and trigger efficiency [32, 33], and in the b -tagging efficiency [34], are treated through correction factors that are derived from data and applied as weights to the simulated events. The MC samples are also reweighted so that the distribution of the average number of interactions per bunch crossing reproduces the observed distribution in the data.

Simulated WW signal samples were produced by summing $q\bar{q}$ - and gg -initiated samples. The $q\bar{q}$ -initiated WW signal was simulated at next-to-leading-order (NLO) accuracy in QCD using the PowHEG Box v2 [35–37] generator interfaced to PYTHIA 8.186 [38] for the modelling of the parton shower, hadronisation, and underlying event, with parameter values set according to the AZNLO tune [39]. The CT10NLO parton distribution function (PDF) set [40] was used for the hard-scattering processes, whereas the CTEQ6L1 PDF set [41] was used for the parton shower [42]. The events were normalised to the cross-section calculated to next-to-next-to-leading order (NNLO) in QCD [43]. Loop-induced $gg \rightarrow WW \rightarrow \ell\nu\ell\nu$ events were simulated at LO with up to one additional parton emission using SHERPA 2.2.2, with virtual QCD corrections provided by the OPENLOOPS library [42, 44–46]. The $gg \rightarrow WW$ process was normalised to its inclusive NLO QCD cross-section [47]. An alternative sample of $q\bar{q} \rightarrow WW$ events was simulated using SHERPA 2.2.2 [42, 48] with matrix elements at NLO accuracy in QCD for up to one additional parton emission and at LO accuracy for up to three additional parton emissions. For the SHERPA $q\bar{q}$ - and gg -initiated samples the NNPDF3.0NNLO set of PDFs was used [49], along with the dedicated set of tuned parton-shower parameters developed by the SHERPA authors. No alternative simulation is considered for the $gg \rightarrow WW$ process, which contributes only a small fraction of the signal.

Table 1 summarises the generators used for the SM backgrounds along with the relevant PDF sets, the set of tuned parameters used to configure the hadronisation and underlying event, and the cross-section order in α_s used to normalise the event yields for these samples. This study uses the same simulated samples and groupings for the SM background processes as the EWK $2\ell+0$ -jets search [22]. The ‘Others’ category groups together processes that produce small or negligible contributions to the signal regions of the search, and includes Drell–Yan, $t\bar{t}+V$ and Higgs boson production. Further information about the simulations of $t\bar{t}$, single-top (Wt), multiboson and boson-plus-jet processes can also be found in the relevant public ATLAS notes [42, 50–52].

Table 1: Simulated background event samples with the corresponding matrix element and parton shower (PS) generators, cross-section order in α_s used to normalise the event yield, underlying-event tune and the generator PDF sets used. Where used, the label ‘V’ refers to a W or Z boson.

Physics process	Generator	Parton shower	Normalisation	Tune	PDF (generator)	PDF (PS)
$t\bar{t}$	POWHEG BOX v2 [36, 37, 53, 54]	PYTHIA 8.230 [55]	NNLO+NNLL [56]	A14 [57]	NNPDF3.0NLO [49]	NNPDF2.3LO [58]
Single top (Wt)	POWHEG BOX v2 [36, 37, 59]	PYTHIA 8.230	NLO+NNLL [60, 61]	A14	NNPDF3.0NLO [49]	NNPDF2.3LO
$VZ = WZ, ZZ$	POWHEG BOX v2 [36, 37, 62, 63]	PYTHIA 8.210	NLO [42, 62, 63]	AZNLO [39]	CT10NLO [40]	CTEQ6L1[64]
‘Others’:						
Higgs	POWHEG BOX v2 [35–37]	PYTHIA 8.212 [55]	NNNLO+NNLL [65–71]	AZNLO [39]	PDF4LHC15NNLO [72]	CTEQ6L1
$V\bar{V}V$	SHERPA 2.2.2 [42, 48, 73]	SHERPA 2.2.2	NLO [42, 48]	SHERPA default [42]	NNPDF3.0NNLO [49]	NNPDF3.0NNLO
$t\bar{t} + H$	MADGRAPH5_AMC@NLO [74]	PYTHIA 8.230 [55]	NLO [65]	A14	NNPDF3.0NLO	NNPDF2.3LO
$t\bar{t} + V$	MADGRAPH5_AMC@NLO	PYTHIA 8.210 [55]	NLO [74, 75]	A14	NNPDF3.0NLO	NNPDF2.3LO
$t\bar{t} + WW$	MADGRAPH5_AMC@NLO	PYTHIA 8.186 [38]	NLO [74]	A14	NNPDF2.3LO	NNPDF2.3LO
$tZ, t\bar{t}t\bar{t}, t\bar{t}t$	MADGRAPH5_AMC@NLO	PYTHIA 8.230	NLO [74]	A14	NNPDF3.0NLO	NNPDF2.3LO
$Z/\gamma(\rightarrow \ell\ell)$ -jets	SHERPA 2.2.1 [48, 73, 76]	SHERPA 2.2.1	NNLO [77]	SHERPA default [76]	NNPDF3.0NNLO	NNPDF3.0NNLO

3.2 Event reconstruction and selection

Events are required to have at least one reconstructed vertex with at least two associated tracks with $p_T > 400$ MeV. When more than one vertex is reconstructed, the one with the highest $\sum p_T^2$ of associated tracks is taken to be the primary vertex. All final-state objects (electrons, muons and jets in this study) are required to satisfy ‘baseline’ criteria to ensure they are well-reconstructed and originate from the primary vertex, and additional ‘signal’ criteria are applied to define the objects used in the measurement. Baseline electrons are required to have $p_T > 10$ GeV, pseudorapidity $|\eta| < 2.47$ and a longitudinal impact parameter z_0 , relative to the primary vertex, satisfying $|z_0 \sin \theta| < 0.5$ mm; baseline muons must fulfill the same criteria except $|\eta| < 2.6$. Electrons must satisfy a *Loose* likelihood-based identification requirement [32], while muons must satisfy the *Medium* identification requirements defined in Ref. [33]. Signal electrons are required to satisfy a *Tight* identification requirement [32] and the track associated with the signal electron is required to have $|d_0|/\sigma(d_0) < 5$, where d_0 is the transverse impact parameter relative to the primary vertex and $\sigma(d_0)$ is its uncertainty, whilst for signal muons the associated track must have $|d_0|/\sigma(d_0) < 3$. The signal-lepton isolation criteria used in the EWK $2\ell+0$ -jets search [22] are also applied in this study. Hadronic jets are reconstructed from energy deposits in topological clusters of calorimeter cells [78, 79] using the anti- k_t algorithm [80], as implemented in the FastJet package [81], with a radius parameter $R = 0.4$. They are then calibrated by the application of a jet energy scale derived from 13 TeV data and simulation [82]. To reduce the effects of pile-up, for jets with $|\eta| < 2.5$ and $p_T < 120$ GeV a significant fraction of the tracks associated with each jet must have an origin compatible with the primary vertex, as defined by the jet vertex tagger [83]. For jets with $|\eta| > 2.5$ and $p_T < 60$ GeV, similar pile-up suppression is achieved through the forward jet vertex tagger [84]. Finally, events are rejected if they contain a jet that does not satisfy the jet-quality requirements [85, 86]; this removes events impacted by detector noise or non-collision backgrounds. Jets containing b -hadrons (‘ b -jets’) are identified by the MV2c10 boosted decision tree algorithm [34], using quantities such as the impact parameters of associated tracks along with well-reconstructed secondary vertices. A selection that provides 85% efficiency for tagging b -jets in simulated $t\bar{t}$ events is used in this study. Only jet candidates with $p_T > 20$ GeV and $|\eta| < 2.4$ are considered,² although all jets with $|\eta| < 4.9$ are included in the calculation of missing transverse momentum and in the procedure to remove reconstruction ambiguities that could lead to double counting of baseline objects. This procedure is applied as follows:

- jet candidates within $\Delta R' = \sqrt{(\Delta y)^2 + (\Delta\phi)^2} = 0.2$ of an electron candidate are removed;

² Hadronic τ -lepton decay products are treated as jets.

- jets with fewer than three tracks that lie within $\Delta R' = 0.4$ of a muon candidate are removed;
- electrons and muons within $\Delta R' = 0.4$ of the remaining jets are discarded, to reject leptons from the decay of b - or c -hadrons;
- electron candidates are rejected if they are found to share an inner-detector track with a muon.

The measurements are performed in events with exactly one signal electron and one signal muon with opposite electric charge and each satisfying $p_T > 25$ GeV, and a veto on additional baseline leptons and hadronic jets. The multiplicities of non- b -tagged jets and b -tagged jets are considered separately in the background estimation for this study: events with exactly one b -tagged jet with a veto on additional non- b -tagged jets are used to estimate and validate the top-quark background. Requirements are also placed on the missing transverse momentum ($\mathbf{p}_T^{\text{miss}}$), which has magnitude E_T^{miss} . This is defined as the negative vector sum of the transverse momenta of all identified physics objects (electrons, photons, muons and jets), plus an additional ‘soft term’ to include low-momentum tracks associated with the primary vertex but not with these physics objects. The E_T^{miss} value is adjusted for the calibration of the selected physics objects [87].

To access a region of phase space similar to the WW control region in the EWK $2\ell+0$ -jets search, additional requirements are placed on the following variables in this study:

- The invariant mass of the dilepton system, $m_{e\mu} > 100$ GeV.
- The magnitude of the missing transverse momentum vector, $E_T^{\text{miss}} \in [60, 80]$ GeV.
- The ‘stransverse mass’ variable, $m_{T2} \in [60, 80]$ GeV [88, 89], with m_{T2} defined as:

$$m_{T2}(\mathbf{p}_{T,1}, \mathbf{p}_{T,2}, \mathbf{p}_T^{\text{miss}}) = \min_{\mathbf{q}_{T,1} + \mathbf{q}_{T,2} = \mathbf{p}_T^{\text{miss}}} \{ \max [m_T(\mathbf{p}_{T,1}, \mathbf{q}_{T,1}), m_T(\mathbf{p}_{T,2}, \mathbf{q}_{T,2})] \},$$

where m_T is the transverse mass defined as $m_T = \sqrt{2 \times |\mathbf{p}_{T,a}| \times |\mathbf{p}_{T,b}| \times (1 - \cos(\Delta\phi))}$, and $\Delta\phi$ is the azimuthal angle between the particles with transverse momenta $\mathbf{p}_{T,a}$ and $\mathbf{p}_{T,b}$. The vectors $\mathbf{p}_{T,1}$ and $\mathbf{p}_{T,2}$ are the transverse momenta of the two leptons, and $\mathbf{q}_{T,1}$ and $\mathbf{q}_{T,2}$ satisfy $\mathbf{p}_T^{\text{miss}} = \mathbf{q}_{T,1} + \mathbf{q}_{T,2}$. The m_{T2} variable was designed to be sensitive to the mass scales of pair-produced heavy particles that each decay semi-invisibly. The minimisation is performed over all the possible decompositions of $\mathbf{p}_T^{\text{miss}}$ into two hypothetical invisible particles with momenta $\mathbf{q}_{T,1}$ and $\mathbf{q}_{T,2}$. For $t\bar{t}$ or WW decays, assuming an ideal detector with perfect momentum resolution, $m_{T2}(\mathbf{p}_{T,\ell_1}, \mathbf{p}_{T,\ell_2}, \mathbf{p}_T^{\text{miss}})$ has a kinematic endpoint at the mass of the W boson [89]. The signal regions of the EWK $2\ell+0$ -jets search required higher values, $m_{T2} > 100$ GeV.

In the EWK $2\ell+0$ -jets search, the top-quark contamination in events with a jet veto was observed to increase with m_{T2} in the region $m_{T2} \in [60, 100]$ GeV. To maximise WW purity, the control region required $m_{T2} \in [60, 65]$ GeV and $E_T^{\text{miss}} \in [60, 100]$ GeV with validation of the estimate being performed in events with $m_{T2} \in [65, 100]$ GeV and $E_T^{\text{miss}} > 60$ GeV. Since m_{T2} is sensitive to the angular separation of the lepton pair, the m_{T2} range is widened for the analysis described in this paper to provide a broader phase space for measuring angular distributions. Since E_T^{miss} and m_{T2} are correlated, the E_T^{miss} range is tightened to reduce the top-quark contamination. These changes increase the number of events in the region used to perform the differential cross-section measurements without reducing the WW purity. The previously used requirement on the ‘object-based E_T^{miss} significance’ [90] is removed to simplify the definition of

the fiducial region at particle level.³ The definition of the signal region used for this measurement is summarised in Table 2. The same selections are used at particle level when defining the fiducial region used for the fiducial and differential cross-section calculations, as discussed in Section 3.4.

Table 2: Summary of the selection criteria used for the signal region in this study. The same selections are used at detector level and particle level.

Selection requirement	Criteria
Lepton flavour	$e^\pm \mu^\mp$
Lepton p_T	$> 25 \text{ GeV}$
Lepton $ \eta $	$< 2.47 (e^\pm), < 2.6 (\mu^\mp)$
Lepton veto	No additional electrons with $p_T > 10 \text{ GeV}, \eta < 2.47$ No additional muons with $p_T > 10 \text{ GeV}, \eta < 2.6$ $> 100 \text{ GeV}$
$m_{e\mu}$	
Jet veto	No jets with $p_T > 20 \text{ GeV}, \eta < 2.4$
m_{T2}	$\in [60, 80] \text{ GeV}$
E_T^{miss}	$\in [60, 80] \text{ GeV}$

Figure 1 shows detector-level comparisons between the data and the SM processes for the six variables that are unfolded to particle level in this study.

³ The ‘object-based E_T^{miss} significance’ helps to separate events with true E_T^{miss} (arising from weakly interacting particles) from those where it is consistent with particle mismeasurement, resolution effects or identification inefficiencies. On an event-by-event basis, given the full event composition, the E_T^{miss} significance evaluates the p -value that the observed E_T^{miss} is consistent with the null hypothesis of zero real E_T^{miss} , as further detailed in Ref. [90].

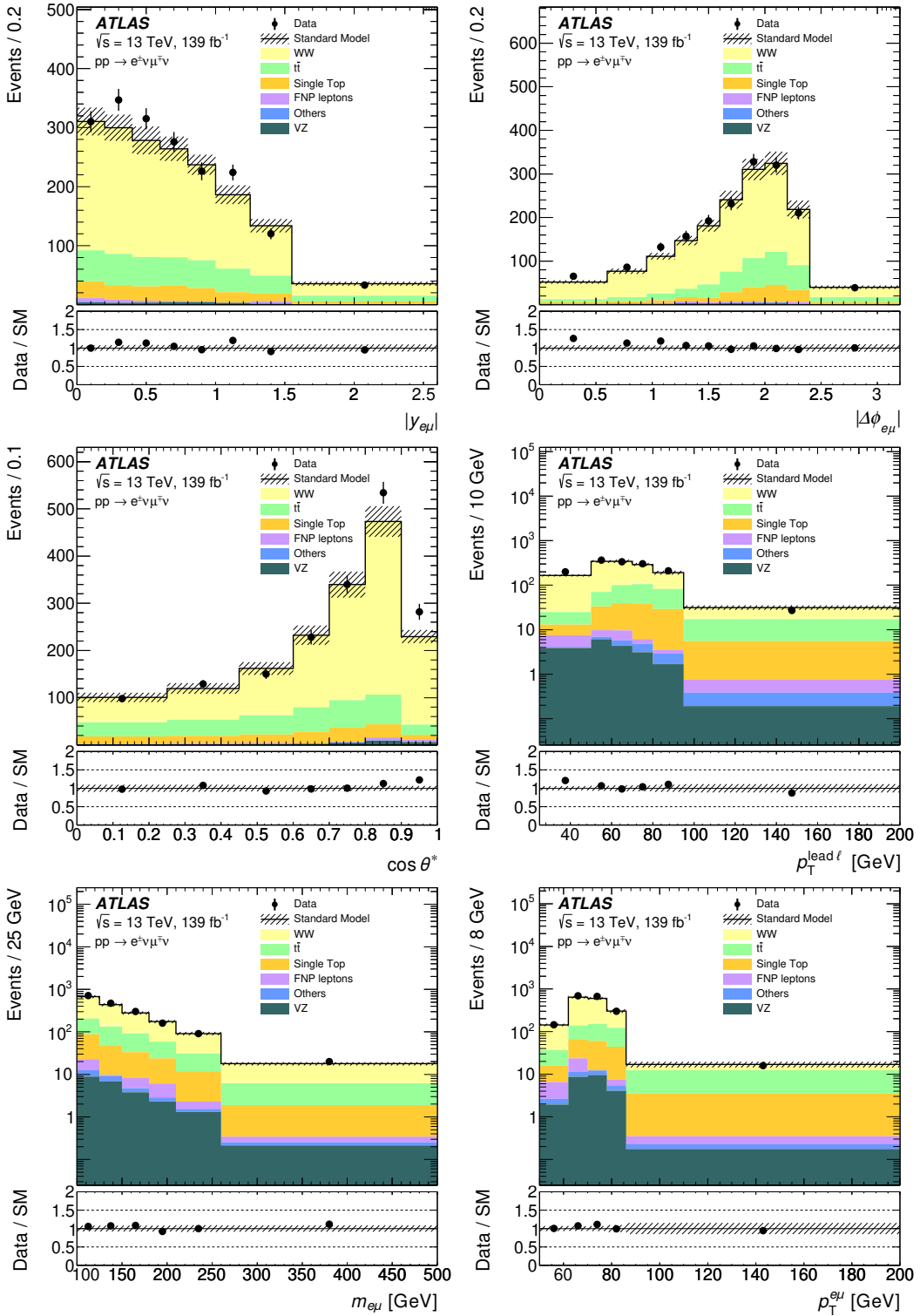


Figure 1: Signal region detector-level distributions of $|y_{e\mu}|$ (top left), $|\Delta\phi_{e\mu}|$ (top right), $\cos\theta^*$ (middle left), $p_T^{\text{lead}\ell}$ (middle right), $m_{e\mu}$ (bottom left), and $p_T^{e\mu}$ (bottom right). Data are indicated by black markers along with the distribution for the WW signal and background SM processes. The last bin of each scale-variable distribution contains overflow events. The lower panels show the ratio of data to the total SM background prediction. The uncertainty bands shown include statistical and systematic uncertainties, excluding theory uncertainties in the WW signal. ‘FNP leptons’ refers to the background from fake/non-prompt leptons, calculated using the data-driven matrix method.

3.3 Background estimation

The estimation of the SM backgrounds in this study uses the same techniques as those used in the EWK $2\ell+0$ -jets search [22]. For the search, the SM backgrounds were classified into irreducible backgrounds from processes producing prompt leptons and reducible backgrounds containing one or more fake/non-prompt (FNP) leptons. The main irreducible backgrounds were SM diboson (WW , WZ , ZZ) and top-quark ($t\bar{t}$ and Wt) production, which were estimated from simulated events and normalised using a simultaneous likelihood fit to data in dedicated control regions (CRs). The yields and shapes of kinematic distributions of the relevant backgrounds were then validated in a set of validation regions (VRs). Three CRs were used: CR- WW , targeting WW production; CR- VZ , targeting WZ and ZZ production, which were normalised by using a single parameter in the likelihood fit to the data; and CR-top, targeting $t\bar{t}$ and single-top-quark production, which were also normalised by using a single parameter in the likelihood fit to the data. Both CR- VZ and CR-top require high m_{T2} , and high values of E_T^{miss} and its significance. CR- VZ uses same-flavour (dielectron and dimuon) events with a jet veto and requires the dilepton invariant mass to be consistent with an on-shell Z boson. CR-top requires one electron and one muon, one b -tagged jet with a veto on additional non- b -tagged jets. The remaining background from FNP leptons was estimated from data using the matrix method [91]. In this study, WW is the target signal process, with the remaining processes being backgrounds that are subtracted from the data prior to calculating the fiducial and differential cross-sections.

The statistical interpretation for the search was performed using the HistFitter framework [92]. The likelihood for the ‘background-only’ fit used to constrain the background normalisation factors was a product of Poisson probability density functions describing the observed number of events in each CR and Gaussian distributions that constrain the nuisance parameters associated with the systematic uncertainties. Poisson distributions were used for MC statistical uncertainties. Further details of the likelihood fit can be found in the EWK $2\ell+0$ -jets search paper [22]. After the fit, the normalisation factors returned for the WW , $t\bar{t}$ and single-top-quark, and WZ/ZZ processes were 1.25 ± 0.11 , 0.82 ± 0.06 and 1.18 ± 0.05 respectively (where the errors include both statistical and systematic uncertainties), which for diboson processes were applied to MC samples scaled to NLO QCD cross-sections (the NNLO QCD cross-sections were not used in the original search paper because the samples were normalised to the data in the control regions). Good agreement, within about one standard deviation, was observed for the yields and kinematic distributions in all VRs when applying these normalisation factors and their corresponding uncertainties. The deviation of the WW normalisation factor from unity by more than 1σ suggests there is tension between the SM and data in the parameter space probed by the search, and this is tested in the present study.

In this study, the normalisation factors from the EWK $2\ell+0$ -jets search are applied directly to the VZ (WZ/ZZ) and top ($t\bar{t}, Wt$) backgrounds that are subtracted from the data when performing the cross-section measurements described in Section 3.4. The uncertainties in the normalisation factors are propagated through the calculation as discussed in Section 3.5. The correlations and constraints that the likelihood fit imposes on the nuisance parameters describing the systematic uncertainties are not applied in this study; the systematic uncertainties are instead assumed to take their nominal values as discussed in Section 3.5. This approach is designed to be conservative, but it has negligible impact on the results because no significant constraints were observed in the EWK $2\ell+0$ -jets search. To validate the use of the original top normalisation factor from the EWK $2\ell+0$ -jets search in the adjusted phase space of this study, an additional validation exercise is performed to check the modelling of the top-quark background in a region with the same selection as in Table 2 but requiring exactly one b -tagged jet. Good agreement is observed across all six distributions considered for differential cross-section measurements, as shown in Figure 2.

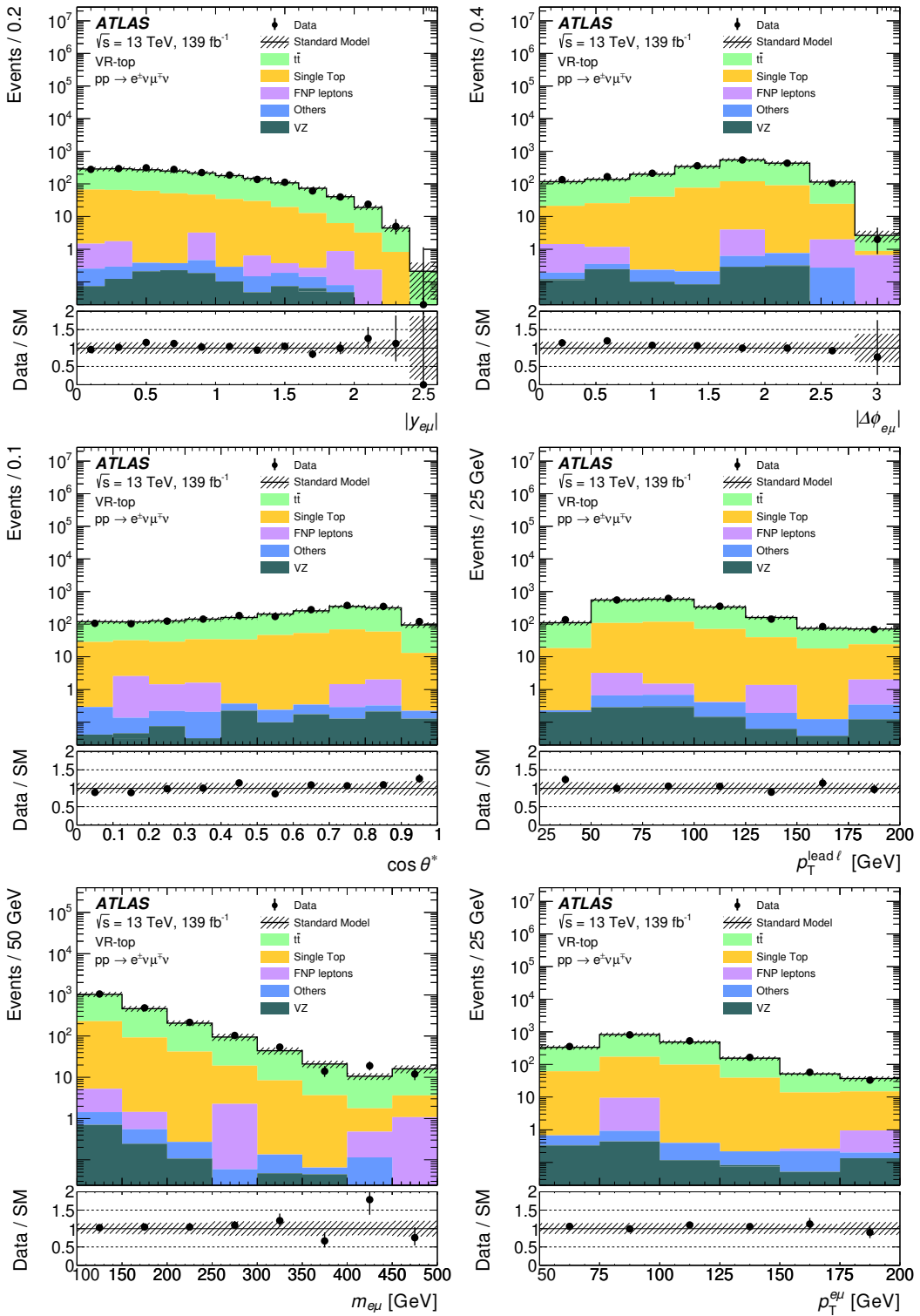


Figure 2: Detector-level distributions of $|y_{e\mu}|$ (top left), $|\Delta\phi_{e\mu}|$ (top right), $\cos\theta^*$ (middle left), $p_T^{\text{lead}\ell}$ (middle right), $m_{e\mu}$ (bottom left), and $p_T^{e\mu}$ (bottom right) in the top validation region. Data are indicated by black markers along with the distribution for the WW signal and background SM processes. The last bin of each scale-variable distribution contains overflow events. The lower panels show the ratio of data to the total SM background prediction. The uncertainty bands shown include statistical and systematic uncertainties, excluding theory uncertainties in the WW signal. ‘FNP leptons’ refers to the background from fake/non-prompt leptons, calculated using the data-driven matrix method.

3.4 Fiducial cross-section determination

The differential cross-sections are measured in the fiducial phase space of the $WW \rightarrow e^\pm \nu \mu^\mp \nu$ decay channel using particle-level implementations of the selection criteria defined in Table 2. The particle-level quantities associated with simulated events are calculated using the SimpleAnalysis [93] framework. The signal particle-level distributions produced by SimpleAnalysis have been validated against the Rivet [94] toolkit that enables further reinterpretation of SM measurements and validation of MC generators. The Rivet routine for this measurement is available on HepData [95].

Electrons and muons are required to originate from the hard interaction and not from hadron decays. Electrons and muons from leptonically decaying τ -leptons are included in the fiducial region. The momenta of photons that are emitted in a cone of size $\Delta R' = 0.1$ around the lepton direction and do not originate from hadron decays are added to form ‘dressed’ leptons. Particle-level jets are reconstructed using the anti- k_t algorithm [80] with radius parameter $R = 0.4$ from visible stable final-state particles, excluding prompt dressed leptons. The particle-level missing transverse momentum is defined as the vectorial sum of the momenta of invisible particles in the event. For SM processes this is the sum of the neutrino momenta.

The fiducial cross-section is calculated as:

$$\sigma_{WW} = \frac{N_{\text{obs}} - N_{\text{bkg}}}{C \cdot \mathcal{L}},$$

where N_{obs} is the observed number of data events in the fiducial region, N_{bkg} is the predicted number of background events, \mathcal{L} the integrated luminosity, and C is a correction factor to account for limited acceptances and detector inefficiencies. It is calculated using MC simulation as the number of simulated signal events passing the detector-level event selection divided by the number of events in the fiducial phase space. In this study, $C = 0.55 \pm 0.08$ is applied, where the uncertainty comes from statistical, experimental and theoretical sources, as described in Section 3.5.

The differential cross-sections are calculated using the iterative Bayesian unfolding (IBU) technique [96, 97] as implemented in the RooUnfold package [98]. This unfolding technique corrects the detector-level distributions of data (with the non- WW backgrounds subtracted) for bin-to-bin migrations due to the event reconstruction. It also applies fiducial corrections (corresponding to events that are reconstructed in the signal region but originate outside the fiducial region at particle level) and reconstruction efficiency corrections (due to events that lie inside the fiducial region at particle level but do not enter the signal region due to detector inefficiencies). The bins chosen for the differential measurements were optimised for a desired level of statistical uncertainty and to reduce the migration of events between particle-level and detector-level bins. The number of iterations used in IBU is also optimised by considering the bias due to the assumed true distribution and the resulting statistical uncertainty of the measurement, with too many iterations generating high statistical uncertainties and too few iterations biasing the measurements towards the MC prediction. In this study, two iterations are chosen for $\cos \theta^*$ and $|\Delta\phi_{e\mu}|$, three iterations are used for $m_{e\mu}$ and $p_T^{\text{lead } \ell}$, and four iterations are used for $|y_{e\mu}|$ and $p_T^{e\mu}$. In addition to the bias tests (discussed in Section 3.5) to measure any systematic effects due to the use of the signal WW MC sample in the unfolding procedure, several signal injection tests were performed using SUSY models for chargino-pair production that were on the edge of the exclusion sensitivity in the EWK 2 ℓ +0-jets search. These are important checks of the validity of using these measurements to calculate constraints on BSM physics. Detector-level distributions of WW plus injected BSM signal were input to the unfolding calculation to test whether the particle-level WW plus BSM distribution could be recovered. The unfolding calculation matched the expected WW plus BSM distributions for a range of SUSY models displaying different kinematics because of their different SUSY particle masses.

3.5 Systematic uncertainties

Systematic uncertainties in the WW differential cross-sections measured in this study arise from experimental sources (which impact the subtracted non- WW backgrounds, and the calculation used to correct the signal for detector effects), uncertainties in the modelling of the top-quark background (which includes theoretical uncertainties, and uncertainties associated with the data-driven background estimate), and signal modelling. Statistical uncertainties associated with the MC samples used for the signal and background processes, and with the observed data distributions, also impact the unfolded distributions.

The sources of experimental uncertainty considered in the EWK $2\ell+0$ -jets search [22] are also considered in this study. The dominant experimental uncertainties are due to the calibration of the jet energy scale and resolution [79, 82]. Additional uncertainties that arise from the lepton reconstruction efficiency, lepton energy scale and lepton energy resolution, and differences between the trigger efficiencies in data and simulation are grouped into the lepton uncertainties category. There are also uncertainties in the scale factors applied to the simulated samples to account for differences between data and simulation in the b -jet identification efficiency, and an uncertainty in $\mathbf{p}_T^{\text{miss}}$ associated with the soft-term resolution and scale [87]. Finally, an uncertainty is assigned to the reweighting procedure (pile-up reweighting) applied to simulated events to match the distribution of the number of interactions per bunch crossing observed in data.

Several sources of uncertainty in the modelling of $t\bar{t}$ and Wt events are accounted for by varying the normalisation and shape of the subtracted backgrounds. For $t\bar{t}$ production, uncertainties in the parton shower simulation are estimated from differences between samples generated with Powheg Box interfaced to either Pythia 8.186 or Herwig 7.04 [99, 100]. Uncertainties in the modelling of initial- and final-state radiation are estimated by comparing the nominal sample with two alternative samples generated with Powheg Box interfaced to Pythia 8.186 but with the radiation settings varied [101]. Finally, an additional uncertainty associated with the choice of event generator is estimated by comparing the nominal samples with samples generated with MadGraph5_AMC@NLO interfaced to Pythia 8.186 [102]. For single-top-quark production, an uncertainty is assigned to the treatment of the interference between the Wt and $t\bar{t}$ samples. This is done by comparing the nominal sample generated using the diagram removal method with a sample generated using the diagram subtraction method [101].

Of the systematic uncertainties considered in the EWK $2\ell+0$ -jets search, uncertainties in the data-driven estimate of FNP leptons and theoretical uncertainties in the diboson WZ/ZZ backgrounds are not applied in this study because these processes contribute little to the subtracted backgrounds. Additional systematic uncertainties are applied to the unfolding to account for the uncertainty in the normalisation of the top-quark and VZ backgrounds, although the VZ normalisation uncertainties are observed to be negligible. The luminosity uncertainty (1.7%) is applied to the subtracted backgrounds that are not estimated using data-driven techniques.

Tests were performed to estimate the bias introduced by using information from the nominal signal MC sample in the unfolding procedure. This includes a data-driven test, whereby MC simulated WW signal events are reweighted at generator level to obtain better agreement between the detector-level signal and the background-subtracted data. The nominal unfolding procedure is then applied to the reweighted detector-level signal distributions to check whether the reweighted particle-level distributions can be reproduced. The impact of theoretical uncertainties in the signal modelling is evaluated by using the detector-level signal distributions with the alternative Sherpa $qq \rightarrow WW$ signal sample introduced in Section 3.1 as input to the nominal unfolding procedure, and comparing the result with the alternative

particle-level signal distribution. In all tests the expected particle-level distributions were accurately recovered so no additional uncertainties were assigned to the unfolding procedure.

Finally, statistical uncertainties from the data are calculated using pseudo-experiments that vary the data distributions according to their Poisson uncertainties in each bin, which are then passed through the unfolding calculation. Statistical uncertainties associated with the simulated MC samples are evaluated using a similar technique.

4 Results

The measured fiducial cross-section for $WW \rightarrow e^\pm \nu \mu^\mp \nu$ production in the phase space defined in Table 2 is:

$$\sigma(WW \rightarrow e^\pm \nu \mu^\mp \nu) = 19.2 \pm 0.3 \text{ (stat)} \pm 2.5 \text{ (syst)} \pm 0.4 \text{ (lumi)} \text{ fb} = 19.2 \pm 2.6 \text{ (total)} \text{ fb}.$$

Of the categories of systematic uncertainties discussed in Section 3.5, the largest contribution is from the experimental jet uncertainty, which contributes a 12% uncertainty to the measured fiducial cross-section. The jet uncertainties are higher than in the previous ATLAS 13 TeV $WW+0$ -jet measurement [15] and this can be attributed to the lower p_T threshold used to define the jet veto. The measured value is compatible with the nominal predictions of 17.8 fb and 17.1 fb from Powheg Box v2 + Pythia 8.186 and Sherpa 2.2.2, respectively, where both are combined with Sherpa 2.2.2 + OpenLoops (LO+PS) for the gg -initiated states. The ratio of the measured cross-section to the nominal Powheg Box v2 + Pythia 8.186 prediction is 1.08. To compare this ratio with the detector-level WW normalisation factor of 1.25 ± 0.11 in the EWK $2\ell+0$ -jets search [22], the former must be multiplied by 1.13 to account for the NLO cross-section calculation, which is included in this study but not in the EWK $2\ell+0$ -jets search. This gives a ratio of 1.22, which is consistent with the normalisation factor from the EWK $2\ell+0$ -jets search.

Particle-level differential cross-sections for the six variables targeted in this study are presented in Figure 3 for the angular variables and Figure 4 for the scale variables. In each case, the right-hand plot shows the impact of the uncertainties, grouped into the categories discussed in Section 3.5, on the measurement.

The dilepton rapidity distribution has a maximum between $|y_{e\mu}| = 0$ and $|y_{e\mu}| = 1$, consistent with central production of a massive diboson system. The $|\Delta\phi_{e\mu}|$ distribution peaks at $|\Delta\phi_{e\mu}| = 2$. The shape of this distribution is influenced by the m_{T2} selection defining the fiducial region: high $|\Delta\phi_{e\mu}|$ values are associated with back-to-back leptons, which typically give lower m_{T2} values than are considered in this study. Conversely, the highest m_{T2} values (which for WW production should occur around 90 GeV in the absence of detector effects) are often associated with collinear leptons (low $|\Delta\phi_{e\mu}|$), which are also excluded from the fiducial region. The $\cos\theta^*$ distribution peaks around $\cos\theta^* = 0.8$, with higher values being suppressed by the rapidity acceptance of the fiducial phase space. The distributions of the scale variables all show the expected characteristic fall for high values of the variable. The fiducial phase-space acceptance also suppresses the leading-lepton and dilepton p_T distributions at lower p_T values.

The measurements are compared with the qq -initiated NLO QCD+PS predictions from Powheg Box v2 + Pythia 8.186 and Sherpa 2.2.2, each combined with Sherpa 2.2.2 + OpenLoops (LO+PS) for the gg -initiated states. For the angular variables, the region with $|\Delta\phi_{e\mu}| < 1.5$ is underestimated by both theory predictions, which is consistent with observations in the previous ATLAS 13 TeV $WW+0$ -jet measurement [15]. The region $\cos\theta^* > 0.8$ is also underestimated by 10%–30% by both predictions. This corresponds to a rapidity difference of $|\Delta y(e\mu)| \geq 2.2$ between the leptons. For the distribution of dilepton

rapidity $|y_{e\mu}|$, the theory shows reasonable agreement with the measurement. The predictions for the scale variables show good agreement with the data except for low values of $p_T^{\text{lead } \ell}$, where both predictions underestimate the cross-section by 20%–25%. Global χ^2 calculations are carried out for all predictions and are displayed in Table 3. Uncertainties in the theory predictions are not considered. The largest χ^2/NDF is 24.1 / 6 corresponding to the comparison between the $q\bar{q} \rightarrow WW$ (SHERPA 2.2.2) + $gg \rightarrow WW$ (SHERPA 2.2.2 + OPENLOOPS) prediction and the unfolded distribution for $p_T^{\text{lead } \ell}$.

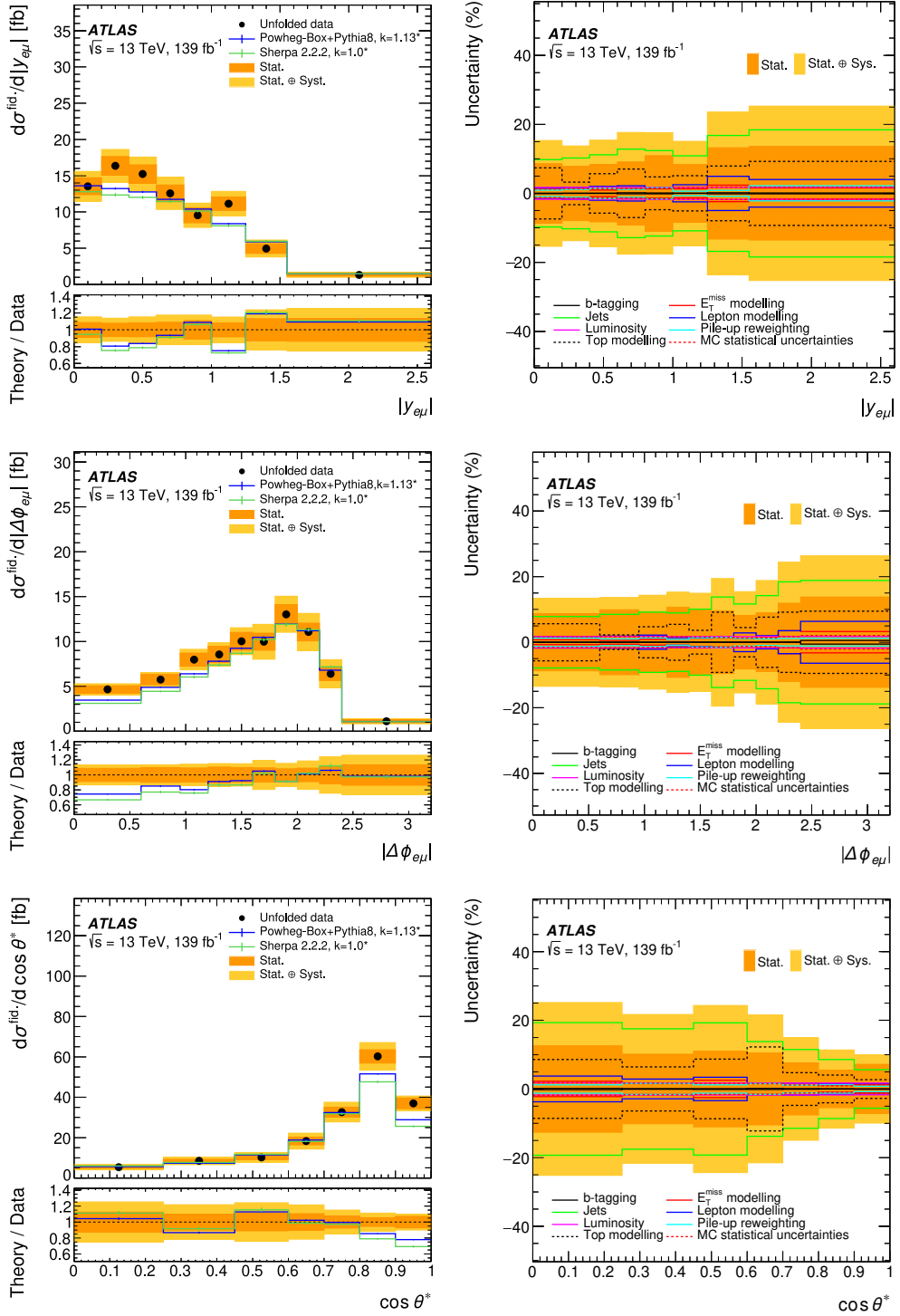


Figure 3: Measured fiducial differential cross-sections of WW production for (top to bottom) $|y_{e\mu}|$, $|\Delta\phi(e\mu)|$ and $\cos\theta^*$. The measured cross-section values are shown as points with dark bands giving the statistical uncertainty and light bands indicating the size of the total uncertainty. The results are compared with the $q\bar{q}$ -initiated predictions from PowHEG Box v2 + PYTHIA 8.186 and SHERPA 2.2.2, each combined with SHERPA 2.2.2 + OPENLOOPS (LO+PS) for the gg -initiated states. The k -factors refer to the corrections applied to scale the predictions of $q\bar{q}$ -initiated and gg -initiated processes to NNLO and NLO accuracy in QCD respectively. The right column shows a breakdown of contributions to the uncertainties in the unfolded measurement.

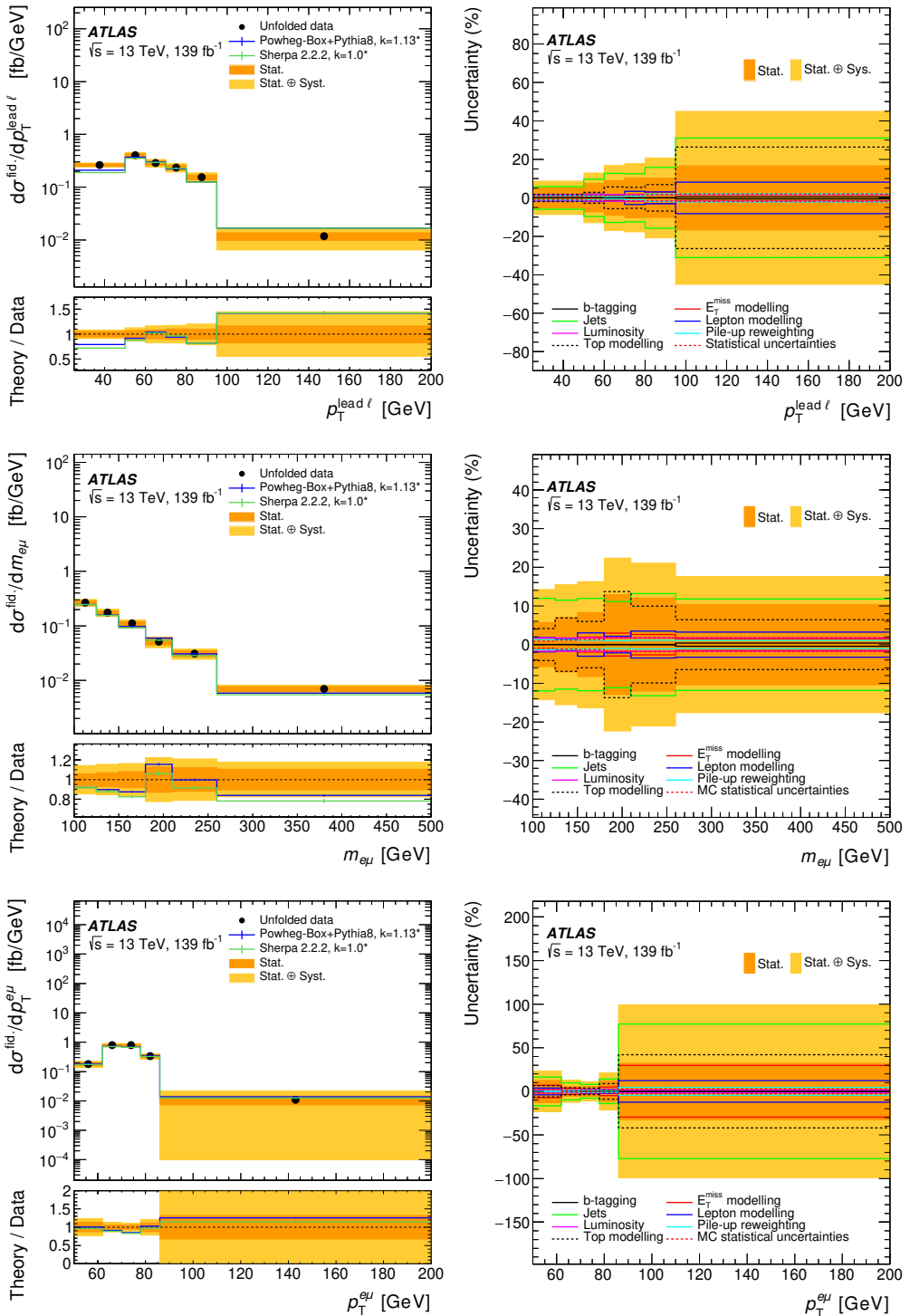


Figure 4: Measured fiducial differential cross-sections of WW production for (top to bottom) $p_T^{\text{lead}\ell}$, $m_{\ell\ell}$ and $p_T^{\ell\ell}$. The last bin is inclusive in the measured observable and for $p_T^{\ell\ell}$ the first bin contains the underflow bin. The measured cross-section values are shown as points with dark bands giving the statistical uncertainty and light bands indicating the size of the total uncertainty. The results are compared with the $q\bar{q}$ -initiated predictions from POWHEG Box v2 + PYTHIA 8.186 and SHERPA 2.2.2, each combined with SHERPA 2.2.2 + OPENLOOPS (LO+PS) for the gg -initiated states. The k -factors refer to the corrections applied to scale the predictions of $q\bar{q}$ -initiated and gg -initiated processes to NNLO and NLO accuracy in QCD respectively. The right column shows a breakdown of contributions to the uncertainties in the unfolded measurement.

Table 3: Chi-squared per number of degrees of freedom χ^2/NDF for a comparison of unfolded distributions with different theory predictions. The calculation takes into account bin-by-bin correlations of systematic and statistical uncertainties. Uncertainties in the theory predictions are not considered.

	$ y_{e\mu} $	$ \Delta\phi_{e\mu} $	$\cos\theta^*$	$p_T^{\text{lead}\ell}$	$m_{e\mu}$	$p_T^{e\mu}$
POWHEG BOX v2 + PYTHIA 8 ($q\bar{q}$) & SHERPA 2.2.2 + OPENLOOPS (gg)	14.4 / 8	10.1 / 10	13.3 / 7	15.4 / 6	2.8 / 6	3.9 / 5
SHERPA 2.2.2 ($q\bar{q}$) & SHERPA 2.2.2 + OPENLOOPS (gg)	18.3 / 8	17.9 / 10	24.5 / 7	24.1 / 6	2.5 / 6	4.1 / 5

5 Conclusion

The cross-section for $WW \rightarrow e^\pm \nu \mu^\mp \nu$ production in pp collisions at $\sqrt{s} = 13$ TeV is measured with the ATLAS detector at the LHC in a fiducial phase-space characterised by the absence of jets and additional leptons, the presence of a high dilepton invariant mass $m_{e\mu}$, and with values of E_T^{miss} and the transverse mass m_{T2} motivated by the control regions used in supersymmetry searches [22]. The measured cross-section is $\sigma(WW \rightarrow e^\pm \nu \mu^\mp \nu) = 19.2 \pm 0.3 \text{ (stat)} \pm 2.5 \text{ (syst)} \pm 0.4 \text{ (lumi)} \text{ fb}$. Differential cross-sections for three variables sensitive to the energy scale of the event and three variables sensitive to the angular correlations of the leptonic decay products are compared with two theoretical SM predictions from perturbative QCD calculations. Good agreement is observed for most distributions within the uncertainties. The largest discrepancies occur at low values of $|\Delta\phi_{e\mu}| < 1.5$, high values of $\cos\theta^* > 0.8$ and low $p_T^{\text{lead}\ell}$, which is consistent with the observations of the previous ATLAS $WW+0$ -jet measurement [15]. This study validates the SM in a new and interesting region motivated particularly by searches for supersymmetry and provides benchmark measurements that can be used to improve future SM predictions and calculate additional constraints on BSM models.

References

- [1] Y. Golfand and E. Likhtman, *Extension of the Algebra of Poincare Group Generators and Violation of P Invariance*, JETP Lett. **13** (1971) 323, [Pisma Zh. Eksp. Teor. Fiz. **13** (1971) 452].
- [2] D. Volkov and V. Akulov, *Is the neutrino a goldstone particle?*, Phys. Lett. B **46** (1973) 109.
- [3] J. Wess and B. Zumino, *Supergauge transformations in four dimensions*, Nucl. Phys. B **70** (1974) 39.
- [4] J. Wess and B. Zumino, *Supergauge invariant extension of quantum electrodynamics*, Nucl. Phys. B **78** (1974) 1.
- [5] S. Ferrara and B. Zumino, *Supergauge invariant Yang-Mills theories*, Nucl. Phys. B **79** (1974) 413.
- [6] A. Salam and J. Strathdee, *Super-symmetry and non-Abelian gauges*, Phys. Lett. B **51** (1974) 353.
- [7] ATLAS Collaboration, *The ATLAS Experiment at the CERN Large Hadron Collider*, JINST **3** (2008) S08003.
- [8] ATLAS Collaboration, *Searches for scalar leptoquarks and differential cross-section measurements in dilepton–dijet events in proton–proton collisions at a centre-of-mass energy of $\sqrt{s} = 13$ TeV with the ATLAS experiment*, Eur. Phys. J. C **79** (2019) 733, arXiv: [1902.00377 \[hep-ex\]](https://arxiv.org/abs/1902.00377).
- [9] ATLAS Collaboration, *Measurement of W^+W^- production in pp collisions at $\sqrt{s} = 7$ TeV with the ATLAS detector and limits on anomalous WWZ and $WW\gamma$ couplings*, Phys. Rev. D **87** (2013) 112001, arXiv: [1210.2979 \[hep-ex\]](https://arxiv.org/abs/1210.2979), Erratum: Phys. Rev. D **88** (2013) 079906.
- [10] CMS Collaboration, *Measurement of the W^+W^- cross section in pp collisions at $\sqrt{s} = 7$ TeV and limits on anomalous $WW\gamma$ and WWZ couplings*, Eur. Phys. J. C **73** (2013) 2610, arXiv: [1306.1126 \[hep-ex\]](https://arxiv.org/abs/1306.1126).
- [11] ATLAS Collaboration, *Measurement of total and differential W^+W^- production cross sections in proton–proton collisions at $\sqrt{s} = 8$ TeV with the ATLAS detector and limits on anomalous triple-gauge-boson couplings*, JHEP **09** (2016) 029, arXiv: [1603.01702 \[hep-ex\]](https://arxiv.org/abs/1603.01702).
- [12] CMS Collaboration, *Measurement of the W^+W^- cross section in pp collisions at $\sqrt{s} = 8$ TeV and limits on anomalous gauge couplings*, Eur. Phys. J. C **76** (2016) 401, arXiv: [1507.03268 \[hep-ex\]](https://arxiv.org/abs/1507.03268).
- [13] ATLAS Collaboration, *Measurement of W^+W^- production in association with one jet in proton–proton collisions at $\sqrt{s} = 8$ TeV with the ATLAS detector*, Phys. Lett. B **763** (2016) 114, arXiv: [1608.03086 \[hep-ex\]](https://arxiv.org/abs/1608.03086).
- [14] ATLAS Collaboration, *Measurement of the W^+W^- production cross section in pp collisions at a centre-of-mass energy of $\sqrt{s} = 13$ TeV with the ATLAS experiment*, Phys. Lett. B **773** (2017) 354, arXiv: [1702.04519 \[hep-ex\]](https://arxiv.org/abs/1702.04519).
- [15] ATLAS Collaboration, *Measurement of fiducial and differential W^+W^- production cross-sections at $\sqrt{s} = 13$ TeV with the ATLAS detector*, Eur. Phys. J. C **79** (2019) 884, arXiv: [1905.04242 \[hep-ex\]](https://arxiv.org/abs/1905.04242).

- [16] ATLAS Collaboration, *Measurements of $W^+W^- + \geq 1$ jet production cross-sections in pp collisions at $\sqrt{s} = 13$ TeV with the ATLAS detector*, *JHEP* **06** (2021) 003, arXiv: [2103.10319 \[hep-ex\]](https://arxiv.org/abs/2103.10319).
- [17] CMS Collaboration, *W^+W^- boson pair production in proton–proton collisions at $\sqrt{s} = 13$ TeV*, *Phys. Rev. D* **102** (2020) 092001, arXiv: [2009.00119 \[hep-ex\]](https://arxiv.org/abs/2009.00119).
- [18] ALEPH, DELPHI, L3 and OPAL Collaborations and the LEP Electroweak Working Group, *Electroweak measurements in electron–positron collisions at W -boson-pair energies at LEP*, *Phys. Rept.* **532** (2013) 119, arXiv: [1302.3415 \[hep-ex\]](https://arxiv.org/abs/1302.3415).
- [19] CDF Collaboration, *Observation of W^+W^- Production in $p\bar{p}$ collisions at $\sqrt{s} = 1.8$ TeV*, *Phys. Rev. Lett.* **78** (1997) 4536.
- [20] CDF Collaboration, *Measurement of the W^+W^- Production Cross Section and Search for Anomalous $WW\gamma$ and WWZ Couplings in $p\bar{p}$ Collisions at $\sqrt{s} = 1.96$ TeV*, *Phys. Rev. Lett.* **104** (2010) 201801, arXiv: [0912.4500 \[hep-ex\]](https://arxiv.org/abs/0912.4500), Erratum: *Phys. Rev. Lett.* **104** (2010) 201801.
- [21] DØ Collaboration, *Measurement of the WW Production Cross Section with Dilepton Final States in $p\bar{p}$ Collisions at $\sqrt{s} = 1.96$ TeV and Limits on Anomalous Trilinear Gauge Couplings*, *Phys. Rev. Lett.* **103** (2009) 191801, arXiv: [0904.0673 \[hep-ex\]](https://arxiv.org/abs/0904.0673).
- [22] ATLAS Collaboration, *Search for electroweak production of charginos and sleptons decaying into final states with two leptons and missing transverse momentum in $\sqrt{s} = 13$ TeV pp collisions using the ATLAS detector*, *Eur. Phys. J. C* **80** (2020) 123, arXiv: [1908.08215 \[hep-ex\]](https://arxiv.org/abs/1908.08215).
- [23] A. J. Barr, *Measuring slepton spin at the LHC*, *JHEP* **02** (2006) 042, arXiv: [hep-ph/0511115](https://arxiv.org/abs/hep-ph/0511115).
- [24] ATLAS Collaboration, *The ATLAS Collaboration Software and Firmware*, ATL-SOFT-PUB-2021-001, 2021, URL: <https://cds.cern.ch/record/2767187>.
- [25] ATLAS Collaboration, *ATLAS data quality operations and performance for 2015–2018 data-taking*, *JINST* **15** (2020) P04003, arXiv: [1911.04632 \[physics.ins-det\]](https://arxiv.org/abs/1911.04632).
- [26] ATLAS Collaboration, *Luminosity determination in pp collisions at $\sqrt{s} = 13$ TeV using the ATLAS detector at the LHC*, ATLAS-CONF-2019-021, 2019, URL: <https://cds.cern.ch/record/2677054>.
- [27] G. Avoni et al., *The new LUCID-2 detector for luminosity measurement and monitoring in ATLAS*, *JINST* **13** (2018) P07017.
- [28] ATLAS Collaboration, *Performance of electron and photon triggers in ATLAS during LHC Run 2*, *Eur. Phys. J. C* **80** (2020) 47, arXiv: [1909.00761 \[hep-ex\]](https://arxiv.org/abs/1909.00761).
- [29] ATLAS Collaboration, *Performance of the ATLAS muon triggers in Run 2*, *JINST* **15** (2020) P09015, arXiv: [2004.13447 \[hep-ex\]](https://arxiv.org/abs/2004.13447).
- [30] ATLAS Collaboration, *The ATLAS Simulation Infrastructure*, *Eur. Phys. J. C* **70** (2010) 823, arXiv: [1005.4568 \[physics.ins-det\]](https://arxiv.org/abs/1005.4568).
- [31] GEANT4 Collaboration, S. Agostinelli et al., *GEANT4 – a simulation toolkit*, *Nucl. Instrum. Meth. A* **506** (2003) 250.

[32] ATLAS Collaboration, *Electron and photon performance measurements with the ATLAS detector using the 2015–2017 LHC proton–proton collision data*, *JINST* **14** (2019) P12006, arXiv: [1908.00005 \[hep-ex\]](#).

[33] ATLAS Collaboration, *Muon reconstruction performance of the ATLAS detector in proton–proton collision data at $\sqrt{s} = 13$ TeV*, *Eur. Phys. J. C* **76** (2016) 292, arXiv: [1603.05598 \[hep-ex\]](#).

[34] ATLAS Collaboration, *ATLAS b -jet identification performance and efficiency measurement with $t\bar{t}$ events in pp collisions at $\sqrt{s} = 13$ TeV*, *Eur. Phys. J. C* **79** (2019) 970, arXiv: [1907.05120 \[hep-ex\]](#).

[35] P. Nason, *A new method for combining NLO QCD with shower Monte Carlo algorithms*, *JHEP* **11** (2004) 040, arXiv: [hep-ph/0409146](#).

[36] S. Frixione, P. Nason and C. Oleari, *Matching NLO QCD computations with parton shower simulations: the POWHEG method*, *JHEP* **11** (2007) 070, arXiv: [0709.2092 \[hep-ph\]](#).

[37] S. Alioli, P. Nason, C. Oleari and E. Re, *A general framework for implementing NLO calculations in shower Monte Carlo programs: the POWHEG BOX*, *JHEP* **06** (2010) 043, arXiv: [1002.2581 \[hep-ph\]](#).

[38] T. Sjöstrand, S. Mrenna and P. Skands, *A brief introduction to PYTHIA 8.1*, *Comput. Phys. Commun.* **178** (2008) 852, arXiv: [0710.3820 \[hep-ph\]](#).

[39] ATLAS Collaboration, *Measurement of the Z/γ^* boson transverse momentum distribution in pp collisions at $\sqrt{s} = 7$ TeV with the ATLAS detector*, *JHEP* **09** (2014) 145, arXiv: [1406.3660 \[hep-ex\]](#).

[40] H.-L. Lai et al., *New parton distributions for collider physics*, *Phys. Rev. D* **82** (2010) 074024, arXiv: [1007.2241 \[hep-ph\]](#).

[41] J. Pumplin et al., *New Generation of Parton Distributions with Uncertainties from Global QCD Analysis*, *JHEP* **07** (2002) 012, arXiv: [hep-ph/0201195](#).

[42] ATLAS Collaboration, *Multi-Boson Simulation for 13 TeV ATLAS Analyses*, ATL-PHYS-PUB-2017-005, 2017, URL: <https://cds.cern.ch/record/2261933>.

[43] T. Gehrmann et al., *W^+W^- Production at Hadron Colliders in Next to Next to Leading Order QCD*, *Phys. Rev. Lett.* **113** (2014) 212001, arXiv: [1408.5243 \[hep-ph\]](#).

[44] F. Buccioni et al., *OpenLoops 2*, *Eur. Phys. J. C* **79** (2019) 866, arXiv: [1907.13071 \[hep-ph\]](#).

[45] F. Caccioli, P. Maierhöfer and S. Pozzorini, *Scattering Amplitudes with Open Loops*, *Phys. Rev. Lett.* **108** (2012) 111601, arXiv: [1111.5206 \[hep-ph\]](#).

[46] A. Denner, S. Dittmaier and L. Hofer, *COLLIER: A fortran-based complex one-loop library in extended regularizations*, *Comput. Phys. Commun.* **212** (2017) 220, arXiv: [1604.06792 \[hep-ph\]](#).

[47] F. Caola, K. Melnikov, R. Röntsch and L. Tancredi, *QCD corrections to W^+W^- production through gluon fusion*, *Phys. Lett. B* **754** (2016) 275, arXiv: [1511.08617 \[hep-ph\]](#).

[48] E. Bothmann et al., *Event generation with Sherpa 2.2*, *SciPost Phys.* **7** (2019) 034, arXiv: [1905.09127 \[hep-ph\]](#).

[49] R. D. Ball et al., *Parton distributions for the LHC run II*, *JHEP* **04** (2015) 040, arXiv: [1410.8849 \[hep-ph\]](https://arxiv.org/abs/1410.8849).

[50] ATLAS Collaboration, *Improvements in $t\bar{t}$ modelling using NLO+PS Monte Carlo generators for Run 2*, ATL-PHYS-PUB-2018-009, 2018, URL: <https://cds.cern.ch/record/2630327>.

[51] ATLAS Collaboration, *Simulation of top-quark production for the ATLAS experiment at $\sqrt{s} = 13$ TeV*, ATL-PHYS-PUB-2016-004, 2016, URL: <https://cds.cern.ch/record/2120417>.

[52] ATLAS Collaboration, *ATLAS simulation of boson plus jets processes in Run 2*, ATL-PHYS-PUB-2017-006, 2017, URL: <https://cds.cern.ch/record/2261937>.

[53] S. Frixione, P. Nason and G. Ridolfi, *A Positive-weight next-to-leading-order Monte Carlo for heavy flavour hadroproduction*, *JHEP* **09** (2007) 126, arXiv: [0707.3088 \[hep-ph\]](https://arxiv.org/abs/0707.3088).

[54] J. M. Campbell, R. K. Ellis, P. Nason and E. Re, *Top-pair production and decay at NLO matched with parton showers*, *JHEP* **04** (2015) 114, arXiv: [1412.1828 \[hep-ph\]](https://arxiv.org/abs/1412.1828).

[55] T. Sjöstrand et al., *An introduction to PYTHIA 8.2*, *Comput. Phys. Commun.* **191** (2015) 159, arXiv: [1410.3012 \[hep-ph\]](https://arxiv.org/abs/1410.3012).

[56] M. Czakon and A. Mitov, *Top++: A program for the calculation of the top-pair cross-section at hadron colliders*, *Comput. Phys. Commun.* **185** (2014) 2930, arXiv: [1112.5675 \[hep-ph\]](https://arxiv.org/abs/1112.5675).

[57] ATLAS Collaboration, *ATLAS Pythia 8 tunes to 7 TeV data*, ATL-PHYS-PUB-2014-021, 2014, URL: <https://cds.cern.ch/record/1966419>.

[58] R. D. Ball et al., *Parton distributions with LHC data*, *Nucl. Phys. B* **867** (2013) 244, arXiv: [1207.1303 \[hep-ph\]](https://arxiv.org/abs/1207.1303).

[59] E. Re, *Single-top Wt-channel production matched with parton showers using the POWHEG method*, *Eur. Phys. J. C* **71** (2011) 1547, arXiv: [1009.2450 \[hep-ph\]](https://arxiv.org/abs/1009.2450).

[60] M. Aliev et al., *HATHOR – HAdronic Top and Heavy quarks crOss section calculatoR*, *Comput. Phys. Commun.* **182** (2011) 1034, arXiv: [1007.1327 \[hep-ph\]](https://arxiv.org/abs/1007.1327).

[61] P. Kant et al., *HATHOR for single top-quark production: Updated predictions and uncertainty estimates for single top-quark production in hadronic collisions*, *Comput. Phys. Commun.* **191** (2015) 74, arXiv: [1406.4403 \[hep-ph\]](https://arxiv.org/abs/1406.4403).

[62] T. Melia, P. Nason, R. Rontsch and G. Zanderighi, *W^+W^- , WZ and ZZ production in the POWHEG BOX*, *JHEP* **11** (2011) 078, arXiv: [1107.5051 \[hep-ph\]](https://arxiv.org/abs/1107.5051).

[63] P. Nason and G. Zanderighi, *W^+W^- , WZ and ZZ production in the POWHEG-BOX-V2*, *Eur. Phys. J. C* **74** (2014) 2702, arXiv: [1311.1365 \[hep-ph\]](https://arxiv.org/abs/1311.1365).

[64] J. Pumplin et al., *New generation of parton distributions with uncertainties from global QCD analysis*, *JHEP* **07** (2002) 012, arXiv: [hep-ph/0201195 \[hep-ph\]](https://arxiv.org/abs/hep-ph/0201195).

[65] D. de Florian et al.,
Handbook of LHC Higgs Cross Sections: 4. Deciphering the Nature of the Higgs Sector, (2016), arXiv: [1610.07922 \[hep-ph\]](https://arxiv.org/abs/1610.07922).

[66] C. Anastasiou et al.,
High precision determination of the gluon fusion Higgs boson cross-section at the LHC, *JHEP* **05** (2016) 058, arXiv: [1602.00695 \[hep-ph\]](https://arxiv.org/abs/1602.00695).

[67] C. Anastasiou, C. Duhr, F. Dulat, F. Herzog and B. Mistlberger,
Higgs Boson Gluon-Fusion Production in QCD at Three Loops, *Phys. Rev. Lett.* **114** (2015) 212001, arXiv: [1503.06056 \[hep-ph\]](https://arxiv.org/abs/1503.06056).

[68] F. Dulat, A. Lazopoulos and B. Mistlberger, *iHixs 2 – Inclusive Higgs cross sections*, *Comput. Phys. Commun.* **233** (2018) 243, arXiv: [1802.00827 \[hep-ph\]](https://arxiv.org/abs/1802.00827).

[69] U. Aglietti, R. Bonciani, G. Degrassi and A. Vicini,
Two-loop light fermion contribution to Higgs production and decays, *Phys. Lett. B* **595** (2004) 432, arXiv: [hep-ph/0404071](https://arxiv.org/abs/hep-ph/0404071).

[70] S. Actis, G. Passarino, C. Sturm and S. Uccirati,
NLO electroweak corrections to Higgs boson production at hadron colliders, *Phys. Lett. B* **670** (2008) 12, arXiv: [0809.1301 \[hep-ph\]](https://arxiv.org/abs/0809.1301).

[71] M. Bonetti, K. Melnikov and L. Tancredi, *Higher order corrections to mixed QCD-EW contributions to Higgs boson production in gluon fusion*, *Phys. Rev. D* **97** (2018) 056017, arXiv: [1801.10403 \[hep-ph\]](https://arxiv.org/abs/1801.10403), Erratum: *Phys. Rev. D* **97** (2018) 099906.

[72] J. Butterworth et al., *PDF4LHC recommendations for LHC Run II*, *J. Phys. G* **43** (2016) 023001, arXiv: [1510.03865 \[hep-ph\]](https://arxiv.org/abs/1510.03865).

[73] T. Gleisberg et al., *Event generation with SHERPA 1.1*, *JHEP* **02** (2009) 007, arXiv: [0811.4622 \[hep-ph\]](https://arxiv.org/abs/0811.4622).

[74] J. Alwall et al., *The automated computation of tree-level and next-to-leading order differential cross sections, and their matching to parton shower simulations*, *JHEP* **07** (2014) 079, arXiv: [1405.0301 \[hep-ph\]](https://arxiv.org/abs/1405.0301).

[75] ATLAS Collaboration,
Modelling of the $t\bar{t}H$ and $t\bar{t}V (V = W, Z)$ processes for $\sqrt{s} = 13$ TeV ATLAS analyses, ATL-PHYS-PUB-2016-005, 2016, URL: <https://cds.cern.ch/record/2120826>.

[76] ATLAS Collaboration, *Monte Carlo Generators for the Production of a W or Z/γ^* Boson in Association with Jets at ATLAS in Run 2*, ATL-PHYS-PUB-2016-003, 2016, URL: <https://cds.cern.ch/record/2120133>.

[77] R. Gavin, Y. Li, F. Petriello and S. Quackenbush,
FEWZ 2.0: A code for hadronic Z production at next-to-next-to-leading order, *Comput. Phys. Commun.* **182** (2011) 2388, arXiv: [1011.3540 \[hep-ph\]](https://arxiv.org/abs/1011.3540).

[78] ATLAS Collaboration,
Topological cell clustering in the ATLAS calorimeters and its performance in LHC Run 1, *Eur. Phys. J. C* **77** (2017) 490, arXiv: [1603.02934 \[hep-ex\]](https://arxiv.org/abs/1603.02934).

[79] ATLAS Collaboration, *Jet energy scale and resolution measured in proton–proton collisions at $\sqrt{s} = 13$ TeV with the ATLAS detector*, *Eur. Phys. J. C* **81** (2020) 689, arXiv: [2007.02645 \[hep-ex\]](https://arxiv.org/abs/2007.02645).

[80] M. Cacciari, G. P. Salam and G. Soyez, *The anti- k_t jet clustering algorithm*, *JHEP* **04** (2008) 063, arXiv: [0802.1189 \[hep-ph\]](#).

[81] M. Cacciari, G. P. Salam and G. Soyez, *FastJet user manual*, *Eur. Phys. J. C* **72** (2012) 1896, arXiv: [1111.6097 \[hep-ph\]](#).

[82] ATLAS Collaboration, *Jet energy scale measurements and their systematic uncertainties in proton–proton collisions at $\sqrt{s} = 13$ TeV with the ATLAS detector*, *Phys. Rev. D* **96** (2017) 072002, arXiv: [1703.09665 \[hep-ex\]](#).

[83] ATLAS Collaboration, *Tagging and suppression of pileup jets with the ATLAS detector*, ATLAS-CONF-2014-018, 2014, URL: <https://cds.cern.ch/record/1700870>.

[84] ATLAS Collaboration, *Forward Jet Vertex Tagging: A new technique for the identification and rejection of forward pileup jets*, ATL-PHYS-PUB-2015-034, 2015, URL: <https://cds.cern.ch/record/2042098>.

[85] ATLAS Collaboration, *Selection of jets produced in 13 TeV proton–proton collisions with the ATLAS detector*, ATLAS-CONF-2015-029, 2015, URL: <https://cds.cern.ch/record/2037702>.

[86] ATLAS Collaboration, *Performance of pile-up mitigation techniques for jets in pp collisions at $\sqrt{s} = 8$ TeV using the ATLAS detector*, *Eur. Phys. J. C* **76** (2016) 581, arXiv: [1510.03823 \[hep-ex\]](#).

[87] ATLAS Collaboration, *Performance of missing transverse momentum reconstruction with the ATLAS detector using proton–proton collisions at $\sqrt{s} = 13$ TeV*, *Eur. Phys. J. C* **78** (2018) 903, arXiv: [1802.08168 \[hep-ex\]](#).

[88] C. G. Lester and D. J. Summers, *Measuring masses of semi-invisibly decaying particles pair produced at hadron colliders*, *Phys. Lett. B* **463** (1999) 99, arXiv: [hep-ph/9906349](#).

[89] A. Barr, C. Lester and P. Stephens, *$m(T2)$: The Truth behind the glamour*, *J. Phys. G* **29** (2003) 2343, arXiv: [hep-ph/0304226](#).

[90] ATLAS Collaboration, *Object-based missing transverse momentum significance in the ATLAS Detector*, ATLAS-CONF-2018-038, 2018, URL: <https://cds.cern.ch/record/2630948>.

[91] ATLAS Collaboration, *Measurement of the top quark-pair production cross section with ATLAS in pp collisions at $\sqrt{s} = 7$ TeV*, *Eur. Phys. J. C* **71** (2011) 1577, arXiv: [1012.1792 \[hep-ex\]](#).

[92] M. Baak et al., *HistFitter software framework for statistical data analysis*, *Eur. Phys. J. C* **75** (2015) 153, arXiv: [1410.1280 \[hep-ex\]](#).

[93] ATLAS Collaboration, *SimpleAnalysis: Truth-level Analysis Framework*, ATL-PHYS-PUB-2022-017, 2022, URL: <http://cds.cern.ch/record/2805991>.

[94] C. Bierlich et al., *Robust Independent Validation of Experiment and Theory: Rivet version 3*, *SciPost Phys.* **8** (2020) 026, arXiv: [1912.05451 \[hep-ph\]](#).

[95] E. Maguire, L. Heinrich and G. Watt, *HEPData: a repository for high energy physics data*, *J. Phys. Conf. Ser.* **898** (2017) 102006, ed. by R. Mount and C. Tull, arXiv: [1704.05473 \[hep-ex\]](#).

[96] G. D’Agostini, *A multidimensional unfolding method based on Bayes’ theorem*, *Nucl. Instrum. Meth. A* **362** (1995) 487, ISSN: 0168-9002.

- [97] G. D'Agostini, *Improved iterative Bayesian unfolding*, (2010), arXiv: [1010.0632 \[physics.data-an\]](https://arxiv.org/abs/1010.0632).
- [98] T. Adye, ‘Unfolding algorithms and tests using RooUnfold’, *Proceedings, 2011 Workshop on Statistical Issues Related to Discovery Claims in Search Experiments and Unfolding (PHYSTAT 2011)* (CERN, Geneva, Switzerland, 17th–20th Jan. 2011) 313, arXiv: [1105.1160 \[physics.data-an\]](https://arxiv.org/abs/1105.1160).
- [99] M. Bähr et al., *Herwig++ physics and manual*, *Eur. Phys. J. C* **58** (2008) 639, arXiv: [0803.0883 \[hep-ph\]](https://arxiv.org/abs/0803.0883).
- [100] J. Bellm et al., *Herwig 7.0/Herwig++ 3.0 release note*, *Eur. Phys. J. C* **76** (2016) 196, arXiv: [1512.01178 \[hep-ph\]](https://arxiv.org/abs/1512.01178).
- [101] ATLAS Collaboration, *Studies on top-quark Monte Carlo modelling for Top2016*, ATL-PHYS-PUB-2016-020, 2016, URL: <https://cds.cern.ch/record/2216168>.
- [102] ATLAS Collaboration, *Studies on top-quark Monte Carlo modelling with Sherpa and MG5_aMC@NLO*, ATL-PHYS-PUB-2017-007, 2017, URL: <https://cds.cern.ch/record/2261938>.